

pubs.acs.org/JACS Article

Interfacial Electric Fields Transform Brown Carbon Formation: Accelerate Radical Coupling toward Strong Light-Absorbing Products

Yangyang Liu, [∇] Kejian Li, [∇] Qiuyue Ge, [∇] Longqian Wang, Wenbo You, Kedong Gong, Jianpeng Ao, Lifang Xie, Wei Wang, Le Yang, Runbo Wang, Jilun Wang, Licheng Wang, Minglu Ma, Tingting Huang, Tao Wang, Minbiao Ji, Hongbo Fu, Jianmin Chen, and Liwu Zhang*



Cite This: https://doi.org/10.1021/jacs.5c08398



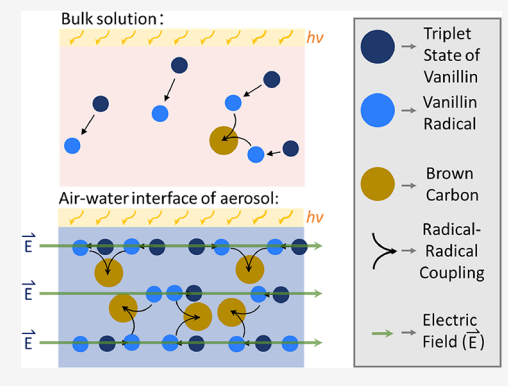
ACCESS

Metrics & More

Article Recommendations

s Supporting Information

ABSTRACT: The formation of brown carbon (BrC) in atmospheric aerosols significantly influences air quality and climate, yet the underlying chemistry governing its interfacial genesis remains poorly understood. Here, we reveal that the intense electric field at the air—water interface of deliquescent nitrite aerosols promotes the oxidation of methoxyphenol, a key biomass burning constituent. The formation of conjugated oligomers, such as $C_{16}H_{14}O_6$ and $C_{15}H_{13}NO_7$, exhibits substantial light absorption (mass absorption coefficients ~4 m² g⁻¹)—a level that surpasses many previously reported pathways. The aging rate can be increased by up to 2 orders of magnitude compared to bulk solutions due to selective radical—radical coupling polymerization. This is driven by promoted intermolecular energy transfer between direction-oriented excited methoxyphenol molecules and reduced energy barriers via stabilized dimer intermediates in the presence of a strong interfacial electric field, as evidenced by high-resolution spectroscopy and quantum



calculations. Our study underscores the catalytic role of electric fields in the browning process, reshaping our understanding of atmospheric photochemical aging and highlighting an overlooked driver of BrC formation with far-reaching implications for aerosol reactivity and atmospheric processes.

■ INTRODUCTION

The atmospheric aerosol functions as a complex chemical reactor, where multiphase processes critically influence chemical constituents that largely regulate air quality, human health, and climate dynamics. 1,2 Among these processes, the formation of light-absorbing organic "brown carbon" (BrC) stands out as a vital yet underexplored facet of atmospheric chemistry.³ One major source of BrC precursors is biomass burning,4 which emits an array of complex mixtures of aromatic compounds (e.g., methoxyphenols) into the atmosphere.⁵ These phenolics undergo complicated photochemical transformations and multiphase aging to produce a secondary organic aerosol,^{6,7} often evolving into light-absorbing species that significantly perturb Earth's radiative balance by absorbing solar radiation in the ultraviolet and visible ranges, contributing to atmospheric warming. Despite their importance, the precise mechanisms driving rapid BrC formation remain poorly understood, creating a critical knowledge gap in our ability to predict atmospheric composition and climate impacts.

A fundamental paradox in atmospheric chemistry has recently emerged: laboratory-measured bulk-phase reaction rates consistently fail to explain the rapid formation of secondary organic aerosols and BrC observed in field studies. 10 This discrepancy suggests the existence of unrecognized acceleration mechanisms operating under real atmospheric conditions. The key to resolving this paradox may lie in revealing the unique physical environments presented by aerosol particles themselves-specifically, the air-water interfaces that dominate their surface chemistry. 11,12 Unlike homogeneous bulk solutions typically studied in laboratories, atmospheric aerosols exhibit remarkably unique features, e.g., extraordinary heterogeneity, steep concentration gradients, and localized pH variations. 13-28 Most intriguingly, these interfaces harbor intense intrinsic electric fields 29-31 (on the order of 10⁷-10⁹ V m⁻¹), created by oriented dipolar molecules and asymmetric ion distributions.³² The interfacial electric field potentially functions as a "natural catalyst", 33 fundamentally altering reaction kinetics, preferred pathways, and product

Received: May 18, 2025 Revised: October 10, 2025 Accepted: October 13, 2025



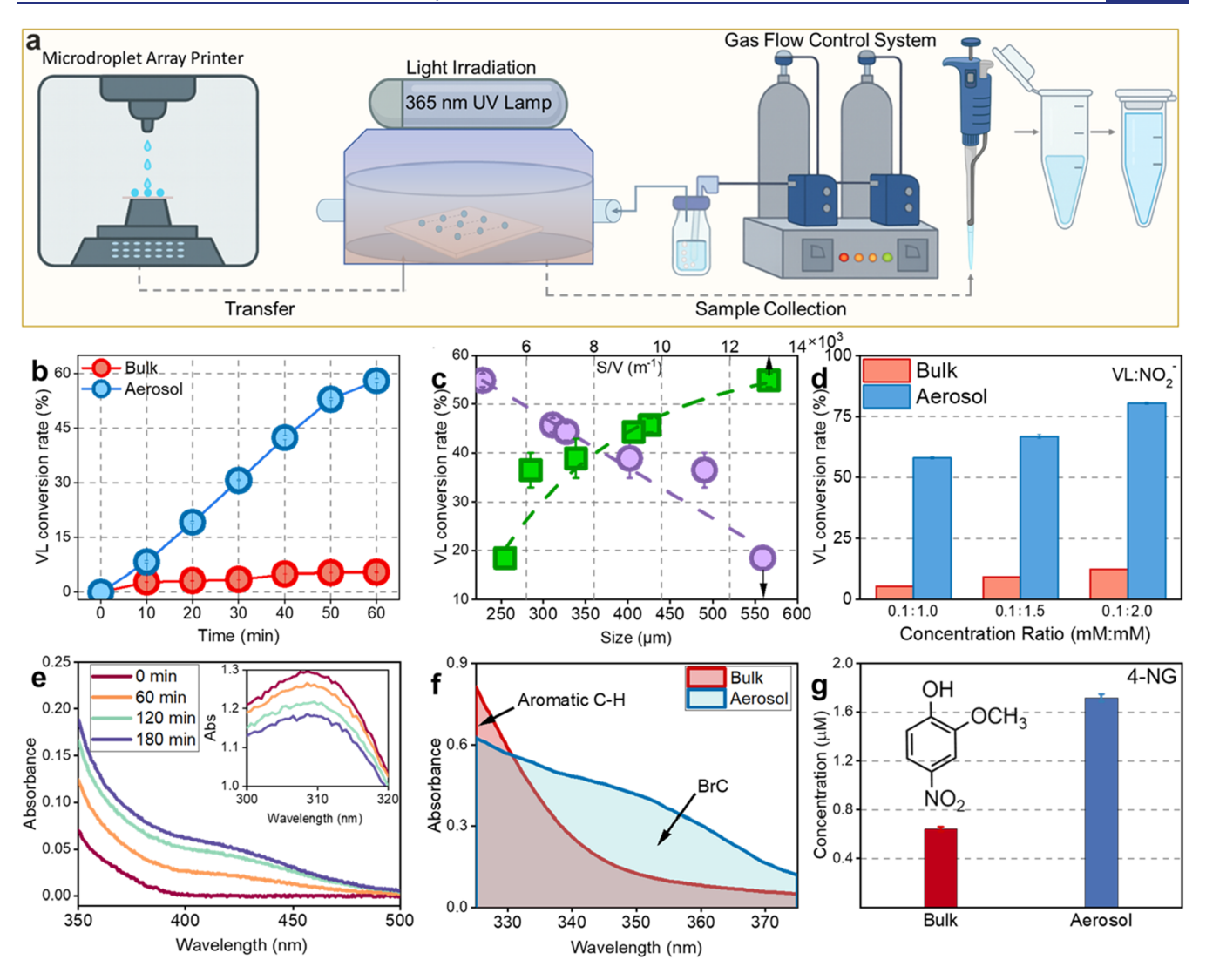


Figure 1. (a) Schematic of the microdroplet aerosol production and collection system, using a custom-designed flow-cell chamber for the reaction of vanillin (VL) with NO_2^- . (b) VL conversion rates with NO_2^- in bulk and aerosol reaction systems, respectively. (c) Size-dependent VL conversion rates: green curve (versus surface-to-volume ratio, S/V, top axis) and purple curve (versus droplet size, bottom x axis). (d) VL conversion rates as a function of the VL: NO_2^- concentration ratio. (e) Time-dependent UV–vis absorption analyses of VL+ NO_2^- bulk phase after photochemical oxidation process. (f) Light absorption properties of VL + NO_2^- after 1 h reaction in bulk solution versus microdroplet aerosol systems. (g) Quantitative analysis of nitroguaiacol (4-NG), a representative brown carbon (BrC) product, in bulk and aerosol systems.

distributions in ways that conventional bulk-phase chemistry cannot replicate. Therefore, interface-driven chemistry represents a "missing link" in our understanding of abnormal atmospheric constitution transformations.

Recall that biomass burning introduces vast quantities of phenolic compounds into the atmosphere, while nitrite (NO_2^{-}) exists as a prevalent aerosol constituent, reaching high concentrations up to ~12.6 μg m⁻³ during pollution episodes.³⁸ This leads to a large possibility of phenolic compounds aged by nitrite aerosol. Notably, nitrite's bent geometry and zero dipole moment allow for preferential orientation at air—water boundaries,³⁹ creating strong interfacial electric fields. Simultaneously, nitrite photolysis generates reactive nitrogen species that drive oxidative transformations.⁴⁰ A critical question emerges: can these intense electric fields at nitrite-enriched interfaces fundamentally reshape the radical chemistry, accelerating BrC formation?

Here, we directly address this critical question by systematically investigating how the interfacial electric fields of nitritecontaining aerosols transform the photochemical oxidation of vanillin—a representative biomass burning methoxyphenol.⁴¹ We first characterize the nitrite spatial distribution and resulting electric field strength within microdroplet aerosols using stimulated Raman scattering microscopy and surfaceenhanced Raman spectroscopy. Next, we demonstrate that these interfacial electric fields accelerate vanillin oxidation by up to 2 orders of magnitude compared to bulk solutions, with reaction rates scaling inversely with microdroplet size. Through high-resolution mass spectrometry, we identify a series of nitrogen-containing oligomeric products that are formed exclusively in the microdroplet environment. Using ultrafast transient absorption spectroscopy and quantum mechanical calculations, we establish that the interfacial electric field fundamentally alters reaction pathways by stabilizing radical intermediates, reducing energy barriers, and promoting selective radical-radical coupling polymerization. These interface-generated brown carbon products exhibit exceptional light absorption properties, with mass absorption coefficients

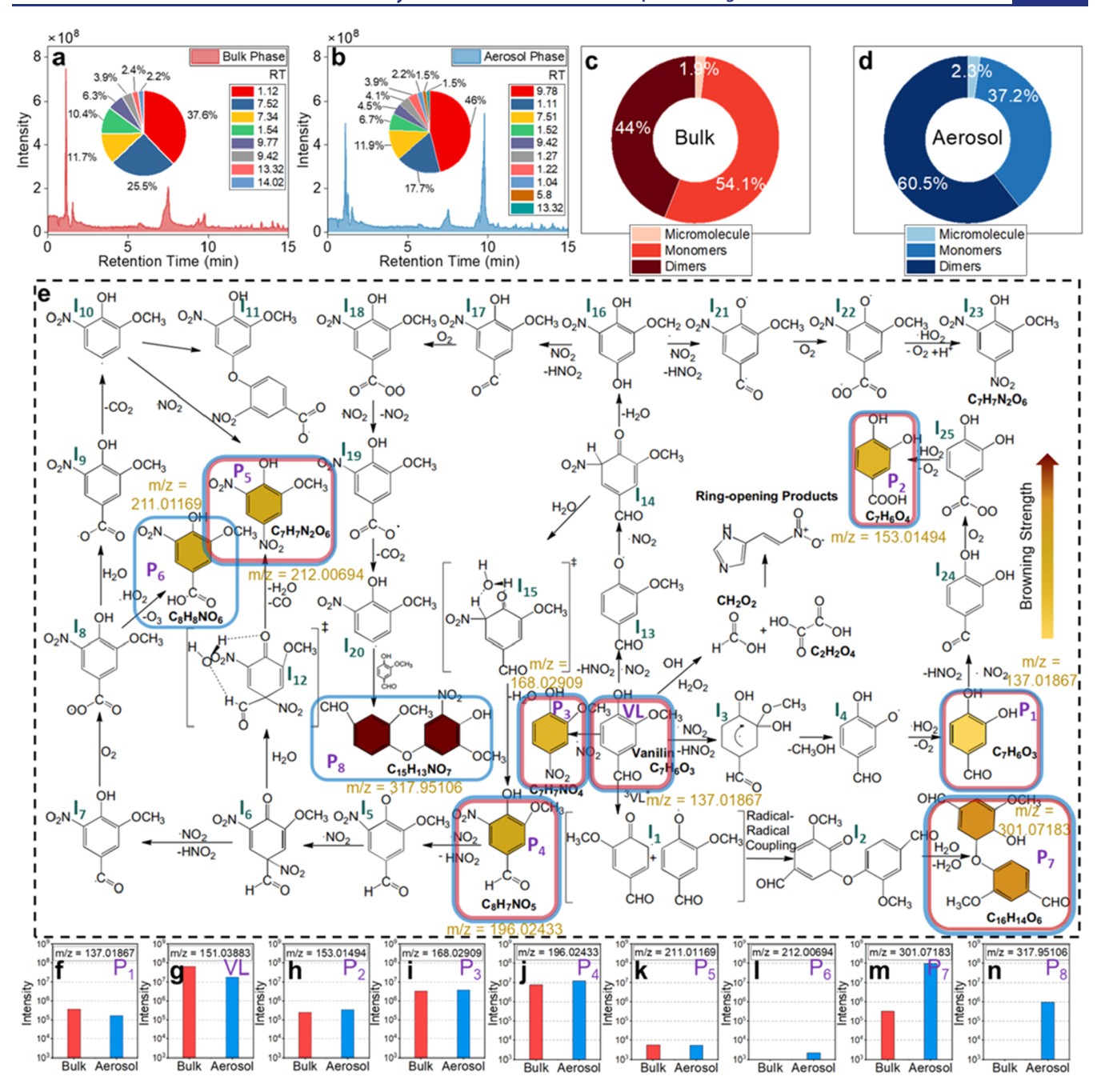


Figure 2. Total ion current (TIC) chromatograms and relative m/z peak abundances from the 180 min photoreaction of vanillin (VL) with NaNO₂ in bulk (a) and aerosol (b) conditions. Relative abundance of small molecules, monomers, and dimers in VL + NO₂⁻ reactions in bulk (c) and aerosol (d) phases, respectively. (e) Proposed mechanisms for major identified products (Table S1) from VL photoreactions with nitrite in bulk and aerosol systems. (f-n) Peak intensities of the eight most abundant m/z products in VL + NO₂⁻ reactions in bulk and aerosol phases. The analysis considered the nine most prominent m/z peaks among the top 15 TIC signals, accounting for >75% of total normalized product abundance.

substantially exceeding some early reported pathways.^{42–56} Our findings reveal that interfacial electric fields function as catalytic forces in atmospheric chemistry, offering a mechanistic explanation for the discrepancy between laboratory and field observations while establishing a fundamental principle with implications extending beyond atmospheric science to diverse areas of chemical reactivity in confined environments.

RESULTS AND DISCUSSION

Nitrite-Mediated Photochemical Oxidation of Vanillin. Photoreactions of microdroplets were performed using a custom-designed reactor (Figure 1a) under high humidity (~93% relative humidity) and 365 nm irradiation (irradiance intensity well covered by UVA range of solar, Figure S1), following our established protocols. ^{57,58} Microdroplet aerosols were generated via an inkjet device, depositing uniform microdroplet arrays onto a superhydrophobic substrate (Figure S2). Figure 1b shows the 1h photochemical oxidation of vanillin (denoted as VL hereafter) mediated by nitrite photolysis in both bulk solution and microdroplet aerosol, and the time-dependent VL depletion rates in nitrite aerosol particles were much higher than those in conventional bulk

conditions, where vanillin oxidation was negligible. After 1 h of irradiation, the nitrite photolysis process results in the depletion of VL by 57.6% in the microdroplet aerosols, in stark contrast to that of 5.51% observed in the bulk case, thus making aging efficiency in microdroplets over 1000% higher than that in the bulk solution. The photochemical oxidation kinetics of VL can be well fitted using quasi-first order, with the corresponding oxidation rates of vanillin in bulk solution and aerosol microdroplets determined to be $1.5 \times 10^{-2} \, \mathrm{min}^{-1}$ and $8.6 \times 10^{-4} \, \mathrm{min}^{-1}$, respectively (Figure S3). These findings reveal a marked acceleration of VL photochemical oxidation in microdroplet aerosols relative to bulk systems, therefore underscoring the distinct role of microdroplet aerosols in triggering an abnormal photochemical aging process in atmospheric aqueous medium.

Recent studies also emphasize the nonmarginal effect of surface-volume (S/V) ratio—directly tied to the abundance of air-water interfaces and thus microdroplet size-on multiphase secondary aerosol formation in the atmosphere. 34,59 We observed a clear size-dependent increase in the depletion rate of vanillin (VL) in nitrite-containing aerosol microdroplets, rising from 19.8% to 53.9% as microdroplet diameter decreased from 559 to 228 μ m, a trend well captured by a growth curve (Figure 1c). Notably, when we only consider the trend for microdroplets below 400 µm in diameter, nitrite aerosol-mediated vanillin photooxidation is surface-areacontrolled and scales linearly with S/V, consistent with the expected interfacial acceleration mechanism recently mapped out using the scaling law^{59,60} (Supporting Discussion 1). Following this trend, atmospheric aerosol particles, typically on the order of a few micrometers or hundreds of nanometers, are likely to accelerate this aging process by up to ~100 times due to significantly increased abundance of the interface. We further explored the effect of nitrite concentration (1, 1.5, and 2 mM), observing a consistent rise in VL depletion rates with increasing nitrite levels in both systems (Figure 1d). In microdroplet aerosols, the photooxidation rate surged from 57.6% to 80.1% as nitrite increased from 1 mM to 2 mM, compared to 5.4% to 12.4% in bulk, attributable to elevated OH and NO2 yields within nitrite aerosol particles (reactions R1-R4).⁶¹ It is worth mentioning that even after 120 min of equilibration at 93% RH, the nitrite increased only slightly, suggesting that solute enrichment due to water evaporation or gas-particle partitioning is a minor contributor to the observed acceleration (<15%) over the time scales relevant to our reaction system (Figure S4, Supporting Discussion 2).

$$NO_2^- + hv \rightarrow NO + O^-$$
 (R1)

$$^{\circ}O^{-} + H^{+} \leftrightarrow ^{\circ}OH$$
 (R2)

$$NO_2^- + OH \rightarrow NO_2 + OH^-$$
 (R3)

$$HNO_2 + OH \rightarrow NO_2 + H_2O$$
 (R4)

Nitrite has been documented as a driver in the nitration of aromatic compounds, yielding brown carbon (BrC) with its light absorption in the ultraviolet—visible (UV—vis) range. Considering this, we examined the nitration of VL mediated by NO_2^- using UV—visible absorption analysis of the bulk solution and aerosol microdroplets after light irradiation (Figure 1e).

In the bulk, relatively low absorbance at 325-450 nm increased with reaction time, reflecting the formation of weak light-absorbing species under illumination (Figure 1f). Upon

1—7 h of light exposure, microdroplets exhibited a marked persistent absorbance enhancement compared to the bulk (Figure S5 and Supporting information 3), corroborated by high-performance liquid chromatography (HPLC) analysis showing elevated 4-nitroguaiacol (4NG) production and yield of nitrogen-containing oligomers only available in microdroplets (detailed in the later section). Besides, similar enhanced light absorption is also observed for emitted biomass burning precursors like catechol, 3-aminophenol, and p-benzoquinone (Figure S6), suggesting that the accelerated browning process in the deliquescent nitrite aerosol is not compound-specific but may extend broadly across emitted biomass burning compounds in the atmosphere (Supporting Discussion 4).

Recall that nitrophenols, such as 4-nitroguaiacol (4NG), are reported to be one of the important sources of atmospheric nitrophenols. Our HPLC analysis quantified 1.70 μ M and 0.65 μ M of 4NG produced in the NO₂⁻-bearing aerosol microdroplets and bulk phase after 1 h of photochemical oxidation (Figure 1g), suggesting the accelerated browning process mediated by aerosol particles. Overall enhancement in light absorption stems from the surface enrichment of NO₂⁻ at the air—water interface and the resulting strong interfacial electric field, which boosts ·NO₂ production and promotes VL polymerization and subsequent nitration—a mechanism elaborated later.

Specification of BrC Constituents and Possible Reaction Pathways. Beyond HPLC trials, we employed ultrahigh-performance liquid chromatography coupled with Q Exactive mass spectrometry (UHPLC-Q Exactive LC-MS) to identify the primary products of NO₂⁻-mediated photolysis of vanillin (VL), elucidating the molecular basis of browning in both bulk and aerosol systems (Figure 2). Product distributions diverged starkly between the two environments (Figure 2a,b), with dimer constituents being more significant under aerosol conditions compared to those in bulk conditions (Figure 2c,d). Products detected in both systems included 4-nitroguaiacol (4NG), 4-hydroxy-3-methoxy-5-nitrobenzalde-hyde, 5-nitrovanillin (5NV), and 5-nitrovanillic acid (5NVA).

Exclusive to microdroplets were 4,6-dinitroguaiacol (DNG) and a nitrated VL dimer derivative (5-nitroguaiacol-4-O-vanillin). These distinct profiles, evidenced by total ion current chromatograms and relative m/z abundances (Figure 2a–d), point to radical-mediated pathways that differ significantly between bulk and aerosol conditions.

The reaction is speculated to commence with the oxidation and nitration of VL, producing the product P_3 (4NG, m/z =168.02909) through the addition of NO2 resulting from the nitrite photolysis process. P_1 compound $(C_7H_6O_3, m/z =$ 137.01867) emerges from intricate processes such as radical nitration with concurrent HNO₂ loss, demethanol, and radicalinduced oxidative transformation, along with the possible formation of intermediates I₃ and I₄. Further experiencing these processes by forming intermediates I24 and I25 leads to the P_2 product ($C_7H_6O_4$, m/z = 153.01494). At the same time, the triplet state of VL (3VL*) underwent an abstraction process to produce VL radicals (I1, denoted as VL), followed by a radical-radical coupling process to form I₂ intermediates, eventually transforming to the stabilized product P7 $(C_{15}H_{14}NO_6, m/z = 301.07183)$. For P_4 $(C_8H_7NO_5, m/z =$ 196.02433), it entails the nitration of I_{13} , where VL reacts with NO₂ and loses HNO₂, followed by a two-step hydration process, forming I_{14} and I_{15} . P_5 ($C_8H_7NO_6$, m/z = 212.01896),

 P_6 (C₇H₆N₂O₆, m/z = 213.0142) and P_8 (C₁₅H₁₃NO₇, m/z =317.95106) come from multiple complicated pathways. One route involves a range of NO2 oxidation and concurrent HNO₂ loss, O₂ oxidation, hydration, and decarboxylation over P₄, which produces I₅-I₁₂ intermediates that essentially contribute to the formation of P₅ and P₆. Intermediate I₁₃ undergoes further nitration to produce I₁₄, a critical node that branches into nitration, O2 addition, hydration, and additional transformations to form a battery of intermediates (I₁₆-I₂₃), eventually driving the formation of P8. The oligomers identified in this study, including the nitrated dimer C₁₅H₁₃NO₇, are consistent with those reported in prior BrC investigations involving phenolic photooxidation and nitration pathways. 3,64,65

Collectively, the microdroplet aerosol yields a unique profile with oxidized products P_6 and P_8 (nitrogen-containing oligomer) detected exclusively in this environment. Besides, the dimer P₇ exhibits substantially higher relative abundance in aerosols. These observations suggest that the abundant airwater interface promotes radical-radical coupling and multistep nitration. These indicate that interfacial forces stabilize reactive intermediates while catalyzing processes such as waterassisted hydrogen rearrangement and NO2 addition, which are essential for forming oxidized species like C₈H₇NO₅ and C₈H₇NO₆.

The Enhanced Light Absorption of BrC Chromophores. The mass absorption coefficient (MAC) of brown carbon (BrC) is a crucial metric for assessing its contribution to atmospheric light absorption and climate effects. 66 Figure 3 compares previously reported and currently determined MAC values across diverse precursor classes, including polycyclic aromatic hydrocarbons (PAHs), 42-46 heterocyclic aromatic, 47-49 VOCs, 43,45 benzenes, 45,50,51 phenol, 43,45,46,52,53 etc. 43,54-56 Spanning 10⁻³ to 10¹ m²g⁻¹, these values reflect the broad variability in light-absorbing properties under differing oxidation and experimental conditions. Aged benzene (toluene) and simple aliphatic VOCs exhibit low MACs (<0.1 m²g⁻¹), indicative of weak near-UV absorption. In contrast, nitration of aromatics (e.g., phenols, PAHs) and multifunctional species display markedly higher MACs (>1 m²g⁻¹), underscoring that nitro group incorporation shifts and intensifies UV-visible absorption, yielding potent atmospheric BrC chromophores.

Vanillin (VL) is a prevalent lignin pyrolysis product in biomass burning emissions,⁶⁷ and it can undergo nitration with nitrite (NO₂⁻) or other nitrogen-containing oxidants, where nitro group addition extends the conjugated system and alters electron distribution within the aromatic ring. 68 This structural shift markedly boosts absorption in the near-UV and extends into the visible range. More strikingly, mediated by nitrite aerosol of the abundant air/water interface, this nitration process yields products of strong light absorption, with MAC values ~4 m² g⁻¹ at 375 nm, approaching or surpassing early reported pathways (e.g., NO_x, OH, and NO_x/OH, Supporting Discussions 5 and 6).

Taken as taken above, mediated by active radical ions and an intense electric field resulting from NO₂-, VL undergoes rapid oxidation, yielding conjugated, nitrogen-containing oligomer products that markedly elevate mass absorption coefficients (MACs). This enhanced aging process generates more absorptive BrC, amplifying the radiative forcing of atmospheric aerosols. Given the ubiquity of phenolic compounds in natural (e.g., biomass burning) and anthropogenic emissions, ⁶⁹ their

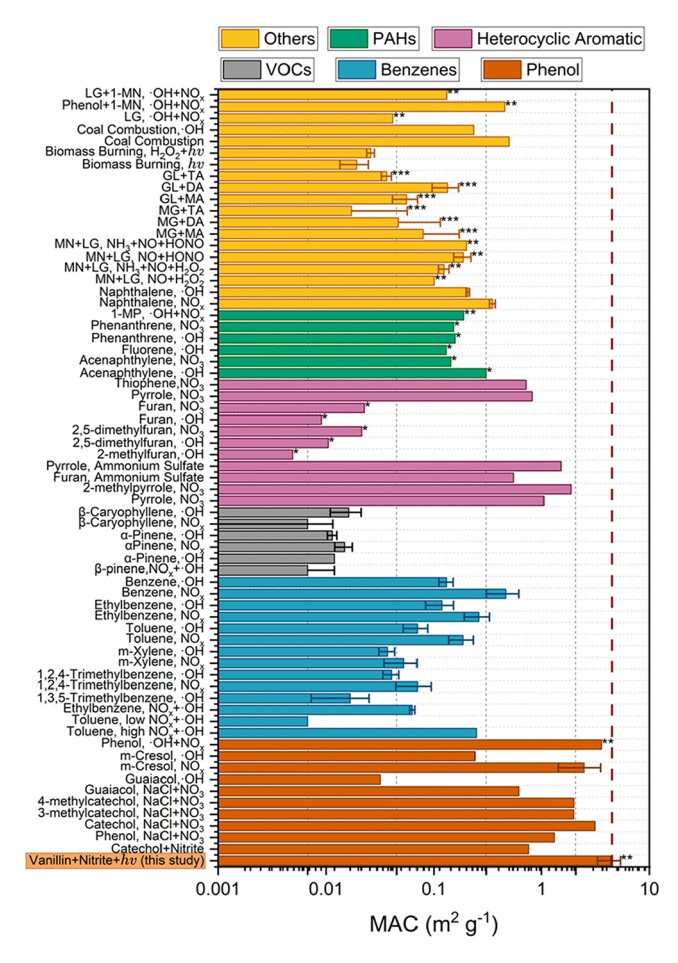


Figure 3. Comparisons for earlier reported and currently determined mass absorption cross section (MAC) values at 365 nm for various organic and inorganic compounds under different oxidation conditions, unless otherwise marked and explained. Data points marked with *, **, and *** denote MAC values measured at 370, 375, and 405 nm, respectively. For compounds with multiple reported values across conditions in the literature, the maximum observed MAC value is presented. Compounds include 1-methylnaphthalene (1-MN), longifolene (LG), methylglyoxal (MG), methylamine (MA), dimethylamine (DA), and trimethylamine (TA). Additional notes are provided in Table S2.

transformation into high-MAC BrC via interface-accelerated photochemical aging likely exerts a substantial influence on regional and global climate. This agrees nicely with very recent illustrations of the dominant contribution of nitrogen-relevant BrC to the overall light absorption on a global scale.⁷⁰

Surface Propensity of Nitrite Ions and Strong Interfacial Electric Field. Adapting our established approach, 14,35,71 we mapped NO₂ distribution in aerosol microdroplets using high-resolution stimulated Raman spectroscopy, collecting $\nu(NO_2^-)$ and $\nu(O-H)$ vibrational modes (Figure 4). The $\nu(NO_2^-)/\nu(O-H)$ ratio served as a proxy for NO₂⁻ concentration in microdroplets generated from 200 mM, 500 mM, and 1,000 mM NO₂ solutions, with sizes on the order of $\sim 20 \mu \text{m}$, $\sim 60 \mu \text{m}$, and $\sim 120 \mu \text{m}$ (Figures S7 and S8). This ratio increased from the microdroplet center to the edge, revealing a pronounced surface propensity of NO2 at the airwater interface, with the enriched zone shrinking as microdroplet sizes enlarge (gray regions). We further quantified this distribution across five concentric, equal-volume regions (0-2%, 20-40%, 40-60%, 60-80%, and 80-100% from center to

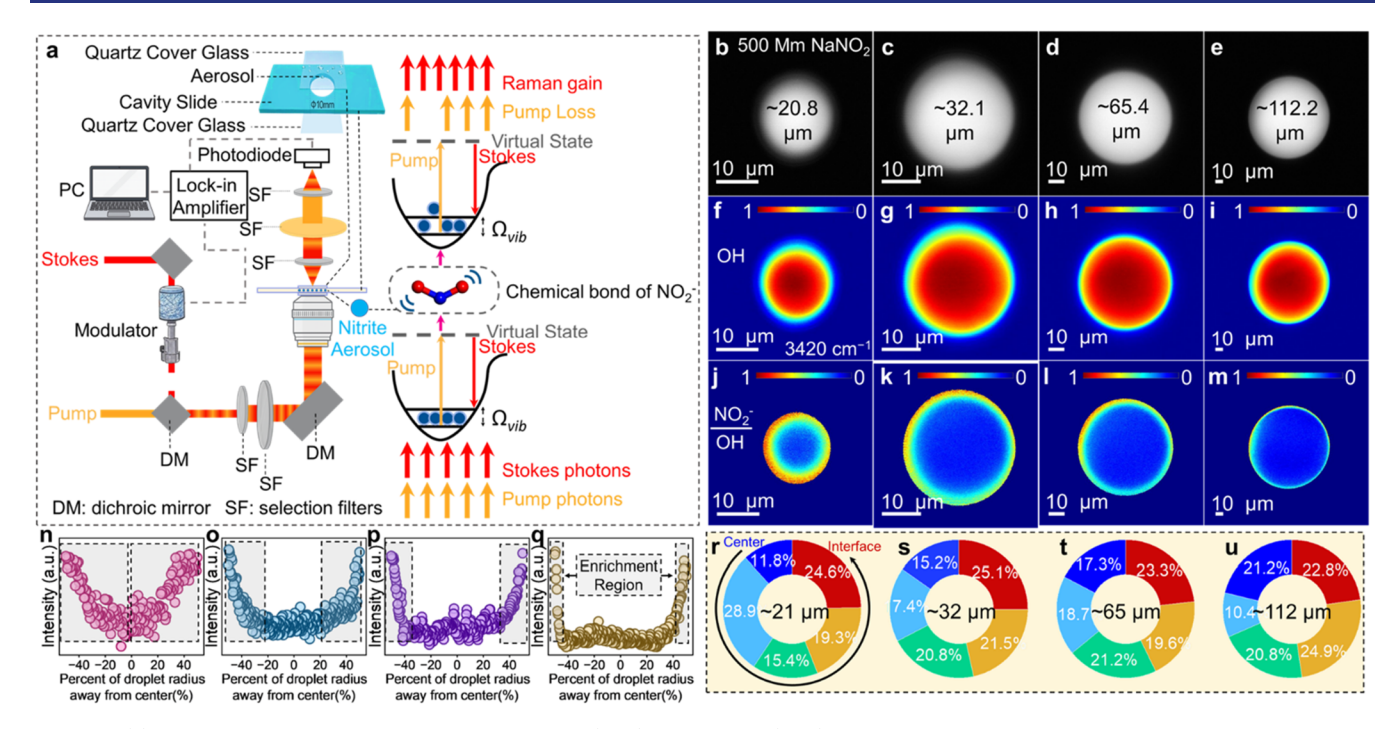


Figure 4. (a) The schematic of stimulated Raman scattering (SRS) microscopy. (b–e) Optical images of NaNO₂ aerosol microdroplets of varying sizes. (f–i) Normalized SRS 2D maps of the O–H vibrational mode, depicting water distribution in NaNO₂ aerosols with diameters of ~20.8, ~32.1, ~65.4, and ~112.2 μ m, respectively. (j–m) Normalized SRS 2D maps of NO₂⁻, using the O–H signal as an internal standard (ν (NO₂⁻)/ ν (O–H)). (n–q) Corresponding line profiles revealing NO₂⁻ enrichment regions within aerosol particles. (r–u) Pie charts quantifying NO₂⁻ distribution across five concentric segments, each comprising 20% of the aerosol sphere volume from edge to center.

edge). The interfacial propensity of NO_2^- correlated strongly with both initial concentration and droplet size: elevating NO_2^- from 200 mM to 1,000 mM enhanced surface enrichment, while at 200 mM, the NO_2^- fraction rose from 10.4% to 16.2% as microdroplet size decreased from ~123 μ m to ~23 μ m (Figure S8).

Differential interfacial affinities of anions and cations establish a double-layer structure, fostering heterogeneous charge distribution and a potent surface electric field.⁷² Leveraging the Stark-sensitive C≡N bond in cyano probes (Figure 5a), we characterized this field in NaNO₂ microdroplet aerosols. The Raman shift of $\nu(C \equiv N)$ decreased progressively from the interface to the center (interface >1/2 > 1/4 >center), revealing a field gradient spanning the microdroplet, with an intense field at the air-water boundary (Figure 5b). Correspondingly, vanillin (VL) oxidation rates in microdroplets (30-87 μ m) were markedly higher at the interface than at the center, aligning with nitrite distribution and field strength. For a \sim 60 μm microdroplet, a $\nu(C \equiv N)$ redshift of 11.55 cm⁻¹—from 2062.49 cm⁻¹ (center) to 2074.04 cm⁻¹ (interface)—indicated an interfacial field of $\sim 3.21 \times 10^7 \text{ V}$ cm⁻¹. Even at the low concentration level of NO₂ (1 mM) and vanillin (0.1 mM), we observed a similar size-dependent electric field strength by adopting concentrated gold nanoparticles (Figures S9 and S10). To fully avoid interference of the SCN probe to determine the electric field of aerosol particles, we adopted the latest approaches monitoring the free OH stretching mode of water in the absence of EF probe and gold nanoparticles³⁰ (Supporting Discussions 7-9). These size-dependent trends (Figures 5c and S11-S13) altogether suggest that in (sub)micron-sized, atmospherically relevant particles (a few micrometers or less), interfacial fields can reach $\sim 10^9$ V cm^{-1.73} Across 30–90 μ m microdroplets, the

interfacial field intensified with decreasing size (Figure 5d). This implies significantly faster VL aging in ambient aerosols than observed under lab conditions. The direct correlation between VL oxidation rates and electric field strength across microdroplet regions underscores this field's pivotal role in regulating photochemical aging.

Mechanistic Insights from Experimental and Theoretical Analyses. O2 is documented to promote photooxidation of organic constituents during the nitrite photolysis process (R5-5₇) by producing ONOO and NO₂ radicals.⁶¹ Switching synthetic air (\sim 21% of the O₂, \sim 79% of the N₂) to pure N₂ (100%) reduced vanillin (VL) depletion (Figure S14), with a more pronounced decrease in the bulk system compared to the aerosol system. This is because VL can efficiently form dimers (e.g., C₁₆H₁₄O₆) even under O₂-free conditions through a radical-radical coupling process in microdroplet aerosol, thus sustaining the reactivity. Notably, enhancing O2 mass transfer via stirring in a bulk system only marginally increased oxidation rates, which remained far below those in microdroplets. 4 This indicates that abundant air—water interfaces contribute minimally to the accelerated VL oxidation in microdroplets by facilitating O2 delivery, pointing to alternative important mechanisms. Nevertheless, secondary reactions involving these *NO2 and *NO3 radicals are modulated by O2 to some extent, leading to the formation of dinitrogen tetroxide (N_2O_4) that boosts $^{\bullet}NO_2$ and $^{\bullet}NO_3$ availability for the subsequent browning process and effectively recycles NO2 through hydrolysis (Supporting Discussions 10 and 11).75-7

$$NO + O_2 \leftrightarrow ONOO$$
 (R5)

$$ONOO' + 'NO \rightarrow N_2O_4$$
 (R6)

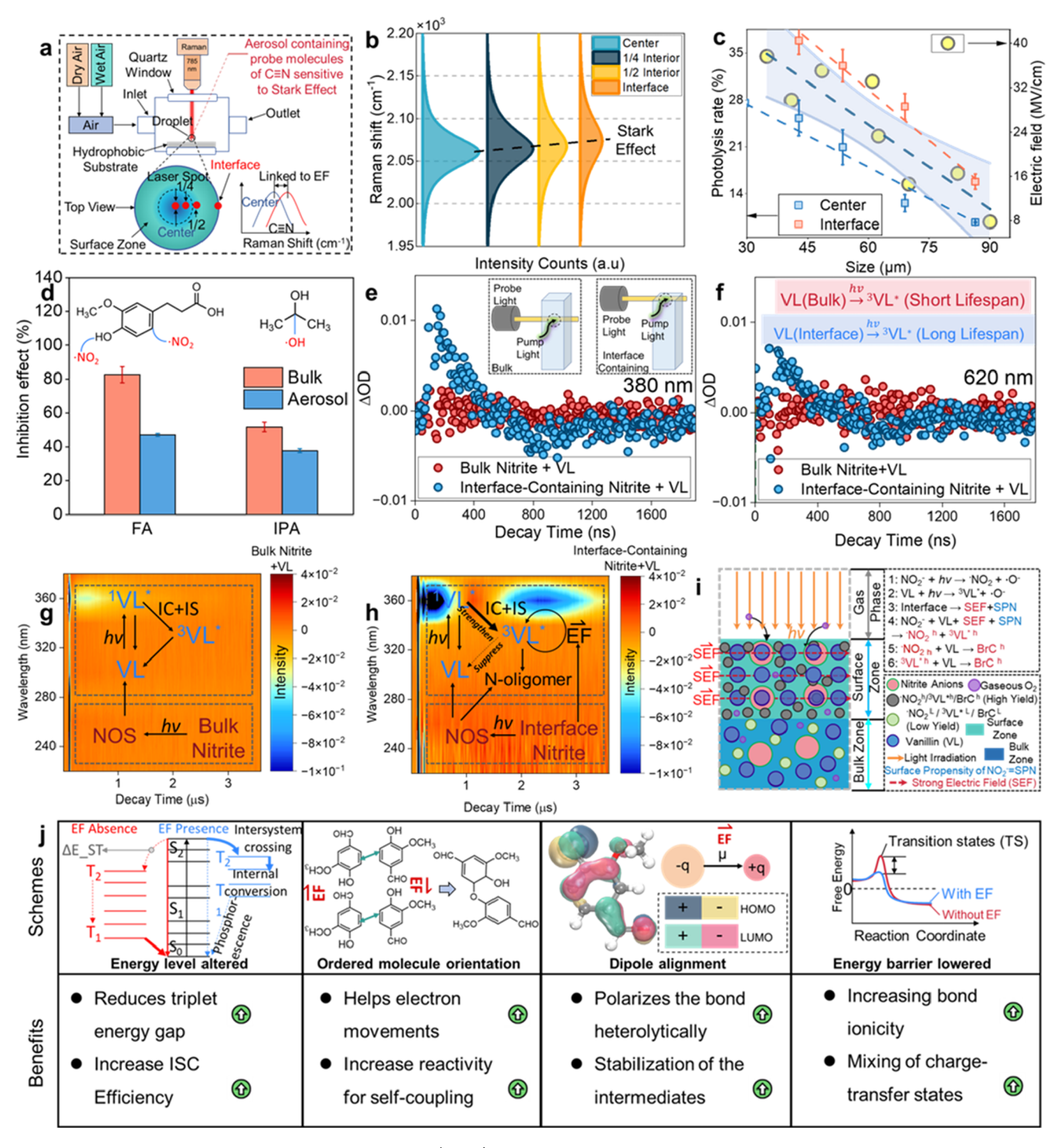


Figure 5. Schematic of surface-enhanced Raman scattering (SERS) with a probe molecule to characterize electric fields in nitrite aerosol particles. (b) Raman analysis of the $\nu(C \equiv N)$ stretching mode across regions of ~60 μ m aerosol microdroplets. (c) Electric field strength profiles across microdroplets of varying sizes. (d) Effects of radical quenchers ferulic acid (FA, ·NO₂) and isopropanol (IPA, ·OH) on vanillin (VL) photolysis rates. (e, f) Nanosecond transient absorption spectra showing decay kinetics of VL-derived products (380 nm) and triplet state (3 VL*, 620 nm) in bulk and interface-rich conditions, with and without NO₂⁻. Full-spectrum transient absorption of NO₂⁻+VL systems in bulk (g) and interface-rich (h) environments; insets denote intersystem crossing (IS), internal conversion (IC), and nitrogen—oxygen species (NOS). (i) Schematic of NO₂⁻+-mediated VL photolysis in aerosol microdroplets. (j) Summarized role of interfacial electric fields in accelerating reaction rates.

$$N_2O_4 \rightarrow 2\dot{N}O_2$$
 (R7)

$$^{\circ}NO_2 + O_2 \rightarrow ^{\circ}NO_3$$
 (R8)

$$N_2O_4 + H_2O \rightarrow HNO_2 + HNO_3$$
 (R9)

Adding 50 μ M ferulic acid (FA) to quench NO₂ reduced vanillin (VL) oxidation rates in bulk and aerosol systems, highlighting NO₂'s critical role in this process. Similarly, 500 mM isopropyl alcohol (IPA) suppressed ·OH-mediated oxidation. Despite these quenchers, VL oxidation persisted at

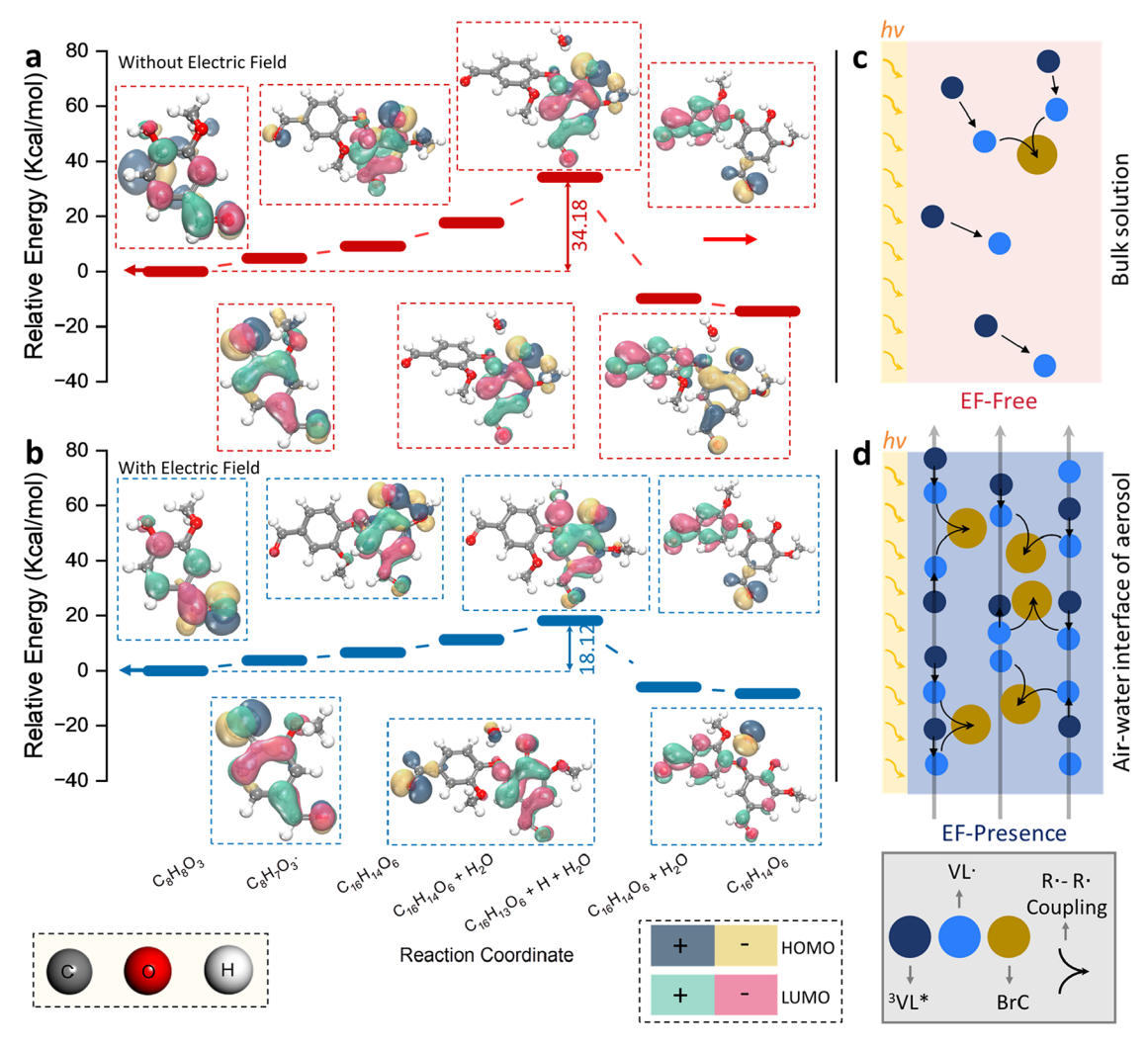


Figure 6. Computed relative energy for photosensitization of VL in the (a) absence and (b) presence of an electric field system as a function of the reaction coordinates. Illustration of different efficiencies of radical—radical coupling in EF-free bulk solution (c) and EF-presence microdroplet aerosol (d). The HOMO (dark grayish blue (+)···light yellow (–) wave function) and LUMO (light mint green (+)···soft pink (–) wave function) are shown with the wave function iso-surfaces plotted at the same isovalue.

4.47% in the bulk and 26.8% in microdroplet aerosols. This stems from an alternative NO₂ production pathway (reactions R5–R7), linked to NO autoxidation:⁷⁸ NO, generated from NO₂⁻, reacts with O₂ to form ONOO⁻, which then combines with NO to yield ONOONO, undergoing homolytic cleavage to produce two NO₂ radicals. Notably, VL preferentially undergoes NO₂-mediated nitration over NO-driven reactions, given NO₂'s higher reactivity with phenolics.⁷⁹ The abundant air—water interface in microdroplets mitigates quenching effects, sustaining higher oxidation rates compared with bulk systems.

Transient absorption analysis at 380 and 620 nm was employed to elucidate the decay kinetics of VL-derived products and the triplet excited state (${}^{3}VL^{*}$) in bulk aqueous and air/water interface-containing systems. ⁸⁰ In control experiments without the addition of VL, no transient signals corresponding to ${}^{3}VL^{*}$ or VL-derived intermediates were detected (Figure S8). The quick quenching process leads to the weak ${}^{3}VL^{*}$ and VL-derived signatures emerging in bulk systems, whereas interface-containing systems of strong electric field exhibited pronounced transient absorption signals (Figure Se,f) due to the efficient production and prolonged lifespan of

these reactive intermediates.⁵⁸ This facilitates the radical-radical coupling process to form oligomers.

In the bulk (Figure 5g), a persistent negative signal centered at 360 nm, lasting $\sim 2~\mu s$, arises from the $^{1}\text{VL*}$ stimulated emission. By contrast, the interface-containing environment promotes internal conversion (IC) and intersystem crossing (IS), driving complex transient absorption dynamics at 360 nm and altering the reactivity of triplet vanillin ($^{3}\text{VL*}$) and facilitating N-oligomer formation (Figure 5h).

From t=0 to ~0.9 μ s, a negative signal arises from ${}^{1}\text{VL}^{*}$ stimulated emission, which is shorter-lived than in the bulk (2 μ s) due to accelerated IS to ${}^{3}\text{VL}^{*}$. Between t=1 and 1.5 μ s, a 0.5 μ s positive signal emerges, attributed to N-oligomer absorption—exclusive to the interface-rich environment—nitro-conjugated oligomers with expanded π -systems having this absorbance. The signal reverts to negative from t=1.5 to 3 μ s, likely due to N-oligomer decay and contributions from ground state bleaching or residual ${}^{1}\text{VL}^{*}$ emission. Namely, the accumulation of a greater number of excited state species, such as the singlet excited state of vanillin (${}^{1}\text{VL}^{*}$), results in a higher population of molecules residing in the excited state due to the presence of the electric field. In this case, a reduction in the

ground state population occurs as more VL molecules are promoted to the excited state.

This leads to decreased absorption at wavelengths corresponding to the ground state absorption band, manifesting as a stronger negative signal in the transient absorption spectrum. These differences underscore an interfacial enhancement driven by localized nitrite accumulation at air—water interfaces, which elevates collision rates between ³VL* and VL, creating reaction hotspots to produce VL radicals. The strong interfacial electric field further promotes intersystem crossing and internal conversion while suppressing radiative decay, thus significantly promoting radical—radical coupling and subsequent nitration, as evidenced by the 360 nm transient absorbance from nitrogen-relevant BrC oligomers. Collectively, the increased yields of reactive intermediates (e.g., ³VL*,·NO₂) due to the interfacial strong electric field drive this accelerated process (Figure 5i).

More specifically, most triplet state vanillin molecules typically return to the ground state through radiative emission (phosphorescence) or nonradiative quenching by solvents or molecular oxygen in the absence of an electric field. However, the electric field narrows the singlet-triplet energy gap ($\Delta E ST$) of vanillin, enhancing the vibronic coupling between these states and boosting the intersystem crossing (ISC) efficiency. This shift diminishes competing radiative pathways, such as phosphorescence, and redirects reactivity (Figure 5j). The potent electric field at microdroplet aerosol interfaces aligns vanillin (VL) molecules and their excited states, orienting the dipoles of polar groups (-CHO and -OH) with the field direction.⁸¹ This orientation enhances intermolecular collision rates and energy transfer efficiency.² Besides, it disrupts the electronic structure and charge distribution of VL and its transition states, directing reaction pathways and altering the kinetics. By amplifying VL's dipole moment, the field stabilizes intermediates (e.g., VL) and transition states, while guiding electron movement and reaction selectivity—reflected in the directional electron-pair shifts of curly arrow mechanisms that dictate bond formation and cleavage.⁸² Beyond this, the electric field further stabilizes ion pairs and polar transition states arising from photoexcitation.⁸³ All of these advantages enhance bond ionicity in transition states, lowering energy barriers, accelerating reactions, and aiding electron extraction from water molecules, as evidenced by the later theoretical calculations.

Figure 6 depicts calculated reaction energy profiles and molecular orbital distribution for the photosensitization of vanillin (VL, C₈H₈O₃) in forming (C₁₆H₁₄O₆) under two conditions: without (Figure 6a) and with (Figure 6c) an electric field, mimicking EF-free bulk and EF-present aerosol environments, respectively. The applied electric field is oriented along the + Z axis and forms an angle with the plane of the aromatic rings. While the reaction axis defined by the C4-C5' bond vector partially lies in the XY plane, vector decomposition gives a positive component along the Z+ direction (Figures S16 and S17, Supporting Discussions 12). This possesses a favorable projection that aligns with the direction of electron flow along the bond-forming coordinate, therefore lowering the reaction barrier by stabilizing the transition state or radical intermediate through the $\mu \cdot E$ interaction mechanism.⁸⁴ In the absence of a field, the photoexcitation of VL generates a singlet excited state that transitions via intersystem crossing to the triplet state (${}^{3}VL^{*}$). Initial hydrogen abstraction from the phenolic - OH group

from randomly arranged VL forms a VL $(C_8H_7O_3)$, overcoming a much higher energy barrier (\sim 34 kcal mol $^{-1}$). These radicals then couple with themselves through a radical–radical interaction, yielding a dimer intermediate $(C_{16}H_{14}O_6)$. Subsequent rearrangement, including aldol condensation between one VL's aldehyde and another's phenolic ring, stabilizes the dimer to derive the final product. The HOMO, only centered on the aromatic ring and methoxy group. This reflects minimal electronic perturbation, driving a slower, controlled reaction dictated by intrinsic molecular properties. In this case, only a small fraction of 3 VL* eventually produces the BrC oligomer through radical–radical coupling (Figure 6c).

Under an electric field simulating aerosol microdroplet environments (Figure 6b), photoexcitation of VL to ³VL* initiates the pathway, with the field reducing the hydrogen abstraction barrier to 18 kcal mol⁻¹, efficiently forming VL. These electric field orientation-directed radicals couple efficiently with each other, eventually yielding C₁₆H₁₄O₆ via a lowered transition state (Figure 6d). Field-enhanced aldol condensation follows, polarizing the aldehyde and phenolic groups to promote nucleophilic addition and dehydration, readily producing the dimer. Final field-driven electron delocalization yields oxidized products, including potential brown carbon (BrC) precursors. The HOMO spreads across the molecular framework, heightening reactivity, while the LUMO focuses on functional groups, enhancing electron acceptance. This polarization lowers excitation energy and boosts photosensitization and radical-radical coupling efficiency, resulting in significantly elevated C₁₆H₁₄O₆ yields in aerosols relative to bulk systems.

Overall, the electric field substantially reduces energy barriers, driving an accelerated pathway. A strong electric field at the air/water interface helps to direct the ordered VL orientation, which enhances charge transfer, hastening bond formation and cleavage. Notably, the $\rm C_{16}H_{14}O_6$ intermediate undergoes rapid hydrogen transfer and rearrangement, propelled by field-augmented electron donation and acceptance. While surface tension and evaporation-confinement effect are plausible drivers in accelerating some reactions in microdroplet aerosol systems, $^{13,84-86}_{13,84-86}$ we elucidate that the strong electric field at the air/water interface of nitrite aerosol is the key driver accelerating BrC formation in the current reaction system (Supporting Discussion 13).

CONCLUSION

ı

Our study unveils a previously overlooked interfacial pathway for brown carbon (BrC) formation that is significant via the intensified radical—radical coupling process over the surface of deliquescent nitrite aerosols. We reveal that the air—water interface of these aerosol particles creates a distinct microenvironment of a strong electric field that markedly accelerates vanillin's photochemical oxidation. A potent interfacial field prolongs the lifetime of reactive triplet states to efficiently produce the radicals and drives coupling polymerization, rapidly forming nitrated conjugated oligomers with exceptional light-absorbing properties.

These findings overturn bulk-phase assumptions, establishing interfacial electric fields as fundamental cornerstones in atmospheric chemistry. The prevalence of phenolic precursors (vanillin, catechol, 3-aminophenol, etc.) in biomass burning emissions suggests this mechanism amplifies BrC production, with nitroaromatic products posing additional toxicity risks and

health concerns (Supporting Discussion 14).87 Our work aligns with emerging insights into nitrogen-relevant BrC (BrN),⁷⁰ spotlighting a critical, overlooked driver of substantial atmospheric reactivity.

This discovery extends beyond atmospheric boundaries, offering fresh perspectives on electric field effects on browning process in volume-confined microdroplet systems—relevant to catalysis, synthetic chemistry, and beyond. As climate-driven wildfires escalate phenolic emissions, intensifying BrC formation and warming feedbacks (Supporting Discussion 15),88 the chemical principles uncovered here demand exploration across diverse aromatics and multiphase contexts. Future studies should probe these synergies to unravel the full scope of interfacial reactivity, promising to reshape our understanding of complex chemical dynamics at air-water boundaries and inspire broad innovative applications in the domains of catalysis, surface science, and organic synthesis.

ASSOCIATED CONTENT

Supporting Information

The Supporting Information is available free of charge at https://pubs.acs.org/doi/10.1021/jacs.5c08398.

> Microdroplet printer photograph; bulk experiment setup; photochemical reaction system; supporting discussion; supporting tables (summary of identified products, summary of reported nitration pathway); and supporting figures (SRS analysis of nitrite aerosol; and transient adsorption spectrum measurement, etc.) (PDF)

AUTHOR INFORMATION

Corresponding Author

Liwu Zhang - Shanghai Key Laboratory of Atmospheric Particle Pollution and Prevention, National Observations and Research Station for Wetland Ecosystems of the Yangtze Estuary, IRDR International Center of Excellence on Risk Interconnectivity and Governance on Weather, Department of Environmental Science & Engineering, Fudan University, Shanghai 200433, Peoples' Republic of China; Shanghai Institute of Pollution Control and Ecological Security, Shanghai 200092, Peoples' Republic of China; o orcid.org/ 0000-0002-0765-8660; Email: zhanglw@fudan.edu.cn

Authors

Yangyang Liu – Shanghai Key Laboratory of Atmospheric Particle Pollution and Prevention, National Observations and Research Station for Wetland Ecosystems of the Yangtze Estuary, IRDR International Center of Excellence on Risk Interconnectivity and Governance on Weather, Department of Environmental Science & Engineering, Fudan University, Shanghai 200433, Peoples' Republic of China; Department of Civil and Environmental Engineering, Virginia Tech, Blacksburg, Virginia 24061, United States; Virginia Tech Institute of Critical Technology and Applied Science (ICTAS), Sustainable Nanotechnology Center (VTSuN), Blacksburg, Virginia 24061, United States

Kejian Li - Shanghai Key Laboratory of Atmospheric Particle Pollution and Prevention, National Observations and Research Station for Wetland Ecosystems of the Yangtze Estuary, IRDR International Center of Excellence on Risk Interconnectivity and Governance on Weather, Department of Environmental Science & Engineering, Fudan University, Shanghai 200433, Peoples' Republic of China

Qiuyue Ge – Shanghai Key Laboratory of Atmospheric Particle Pollution and Prevention, National Observations and Research Station for Wetland Ecosystems of the Yangtze Estuary, IRDR International Center of Excellence on Risk Interconnectivity and Governance on Weather, Department of Environmental Science & Engineering, Fudan University, Shanghai 200433, Peoples' Republic of China

Longqian Wang - Shanghai Key Laboratory of Atmospheric Particle Pollution and Prevention, National Observations and Research Station for Wetland Ecosystems of the Yangtze Estuary, IRDR International Center of Excellence on Risk Interconnectivity and Governance on Weather, Department of Environmental Science & Engineering, Fudan University, Shanghai 200433, Peoples' Republic of China

Wenbo You – Shanghai Key Laboratory of Atmospheric Particle Pollution and Prevention, National Observations and Research Station for Wetland Ecosystems of the Yangtze Estuary, IRDR International Center of Excellence on Risk Interconnectivity and Governance on Weather, Department of Environmental Science & Engineering, Fudan University, Shanghai 200433, Peoples' Republic of China

Kedong Gong – Shanghai Key Laboratory of Atmospheric Particle Pollution and Prevention, National Observations and Research Station for Wetland Ecosystems of the Yangtze Estuary, IRDR International Center of Excellence on Risk Interconnectivity and Governance on Weather, Department of Environmental Science & Engineering, Fudan University, Shanghai 200433, Peoples' Republic of China; Department of Chemistry and Biochemistry, University of California San Diego, San diego, California 92093, The United States of America; o orcid.org/0000-0003-2460-4370

Jianpeng Ao – State Key Laboratory of Surface Physics and Department of Physics, Fudan University, Shanghai 200092, People's Republic of China

Lifang Xie — Shanghai Key Laboratory of Atmospheric Particle Pollution and Prevention, National Observations and Research Station for Wetland Ecosystems of the Yangtze Estuary, IRDR International Center of Excellence on Risk Interconnectivity and Governance on Weather, Department of Environmental Science & Engineering, Fudan University, Shanghai 200433, Peoples' Republic of China

Wei Wang - Shanghai Key Laboratory of Atmospheric Particle Pollution and Prevention, National Observations and Research Station for Wetland Ecosystems of the Yangtze Estuary, IRDR International Center of Excellence on Risk Interconnectivity and Governance on Weather, Department of Environmental Science & Engineering, Fudan University, Shanghai 200433, Peoples' Republic of China

Le Yang - Shanghai Key Laboratory of Atmospheric Particle Pollution and Prevention, National Observations and Research Station for Wetland Ecosystems of the Yangtze Estuary, IRDR International Center of Excellence on Risk Interconnectivity and Governance on Weather, Department of Environmental Science & Engineering, Fudan University, Shanghai 200433, Peoples' Republic of China

Runbo Wang – Shanghai Key Laboratory of Atmospheric Particle Pollution and Prevention, National Observations and Research Station for Wetland Ecosystems of the Yangtze Estuary, IRDR International Center of Excellence on Risk Interconnectivity and Governance on Weather, Department of

- Environmental Science & Engineering, Fudan University, Shanghai 200433, Peoples' Republic of China
- Jilun Wang Shanghai Key Laboratory of Atmospheric
 Particle Pollution and Prevention, National Observations and
 Research Station for Wetland Ecosystems of the Yangtze
 Estuary, IRDR International Center of Excellence on Risk
 Interconnectivity and Governance on Weather, Department of
 Environmental Science & Engineering, Fudan University,
 Shanghai 200433, Peoples' Republic of China
- Licheng Wang Shanghai Key Laboratory of Atmospheric Particle Pollution and Prevention, National Observations and Research Station for Wetland Ecosystems of the Yangtze Estuary, IRDR International Center of Excellence on Risk Interconnectivity and Governance on Weather, Department of Environmental Science & Engineering, Fudan University, Shanghai 200433, Peoples' Republic of China; Occid.org/0000-0002-7290-3255
- Minglu Ma Shanghai Key Laboratory of Atmospheric Particle Pollution and Prevention, National Observations and Research Station for Wetland Ecosystems of the Yangtze Estuary, IRDR International Center of Excellence on Risk Interconnectivity and Governance on Weather, Department of Environmental Science & Engineering, Fudan University, Shanghai 200433, Peoples' Republic of China
- Tingting Huang Shanghai Key Laboratory of Atmospheric Particle Pollution and Prevention, National Observations and Research Station for Wetland Ecosystems of the Yangtze Estuary, IRDR International Center of Excellence on Risk Interconnectivity and Governance on Weather, Department of Environmental Science & Engineering, Fudan University, Shanghai 200433, Peoples' Republic of China
- Tao Wang Shanghai Key Laboratory of Atmospheric Particle Pollution and Prevention, National Observations and Research Station for Wetland Ecosystems of the Yangtze Estuary, IRDR International Center of Excellence on Risk Interconnectivity and Governance on Weather, Department of Environmental Science & Engineering, Fudan University, Shanghai 200433, Peoples' Republic of China; ⊚ orcid.org/0000-0001-9137-5243
- Minbiao Ji State Key Laboratory of Surface Physics and Department of Physics, Fudan University, Shanghai 200092, People's Republic of China; orcid.org/0000-0002-9066-4008
- Hongbo Fu Shanghai Key Laboratory of Atmospheric Particle Pollution and Prevention, National Observations and Research Station for Wetland Ecosystems of the Yangtze Estuary, IRDR International Center of Excellence on Risk Interconnectivity and Governance on Weather, Department of Environmental Science & Engineering, Fudan University, Shanghai 200433, Peoples' Republic of China; ⊚ orcid.org/0000-0002-9492-4452
- Jianmin Chen Shanghai Key Laboratory of Atmospheric Particle Pollution and Prevention, National Observations and Research Station for Wetland Ecosystems of the Yangtze Estuary, IRDR International Center of Excellence on Risk Interconnectivity and Governance on Weather, Department of Environmental Science & Engineering, Fudan University, Shanghai 200433, Peoples' Republic of China; orcid.org/0000-0001-5859-3070

Complete contact information is available at: https://pubs.acs.org/10.1021/jacs.5c08398

Author Contributions

VY.L., K.L., and Q.G. contributed equally to this work.

Notes

The authors declare no competing financial interest.

ACKNOWLEDGMENTS

The authors gratefully acknowledge financial support from the National Natural Science Foundation of China (No. 22376028, No. 22176036, No. 21976030, No. 22006020, No. 223B2601) and the Natural Science Foundation of Shanghai (No. 19ZR1471200).

REFERENCES

- (1) Bikkina, S.; Andersson, A.; Kirillova, E. N.; Holmstrand, H.; Tiwari, S.; Srivastava, A. K.; Bisht, D. S.; Gustafsson, O. Air quality in megacity Delhi affected by countryside biomass burning. *Nat. Sustainability* **2019**, *2* (3), 200–205.
- (2) Liu, T.; Abbatt, J. P. Oxidation of sulfur dioxide by nitrogen dioxide accelerated at the interface of deliquesced aerosol particles. *Nat. Chem.* **2021**, *13* (12), 1173–1177.
- (3) Laskin, A.; Laskin, J.; Nizkorodov, S. A. Chemistry of atmospheric brown carbon. *Chem. Rev.* 2015, 115 (10), 4335–4382.
- (4) Liang, Z.; Zhou, L.; Chang, Y.; Qin, Y.; Chan, C. K. Biomass-burning organic aerosols as a pool of atmospheric reactive triplets to drive multiphase sulfate formation. *Proc. Natl. Acad. Sci. U.S.A.* **2024**, 121 (51), No. e2416803121.
- (5) Akherati, A.; He, Y.; Coggon, M. M.; Koss, A. R.; Hodshire, A. L.; Sekimoto, K.; Warneke, C.; De Gouw, J.; Yee, L.; Seinfeld, J. H.; et al. Oxygenated aromatic compounds are important precursors of secondary organic aerosol in biomass-burning emissions. *Environ. Sci. Technol.* 2020, 54 (14), 8568–8579.
- (6) Liang, Z.; Li, Y.; Go, B. R.; Chan, C. K. Complexities of Photosensitization in Atmospheric Particles. ACS ES T Air 2024, 1 (11), 1333–1351.
- (7) Zhou, L.; Liang, Z.; Qin, Y.; Chan, C. K. Evaporation-Induced Transformations in Volatile Chemical Product-Derived Secondary Organic Aerosols: Browning Effects and Alterations in Oxidative Reactivity. *Environ. Sci. Technol.* **2024**, *58* (25), 11105–11117.
- (8) Palm, B. B.; Peng, Q.; Fredrickson, C. D.; Lee, B. H.; Garofalo, L. A.; Pothier, M. A.; Kreidenweis, S. M.; Farmer, D. K.; Pokhrel, R. P.; Shen, Y.; et al. Quantification of organic aerosol and brown carbon evolution in fresh wildfire plumes. *Proc. Natl. Acad. Sci. U.S.A.* **2020**, 117 (47), 29469–29477.
- (9) Liu, Y.; Wang, T.; Fang, X.; Deng, Y.; Cheng, H.; Bacha, A.-U.-R.; Nabi, I.; Zhang, L. Brown carbon: An underlying driving force for rapid atmospheric sulfate formation and haze event. *Sci. Total Envrion.* **2020**, 734, No. 139415.
- (10) Ervens, B.; Turpin, B.; Weber, R. Secondary organic aerosol formation in cloud droplets and aqueous particles (aqSOA): a review of laboratory, field and model studies. *Atmos. Chem. Phys.* **2011**, *11* (21), 11069–11102.
- (11) Ge, Q.; Liu, Y.; You, W.; Wang, W.; Li, K.; Ruan, X.; Xie, L.; Wang, T.; Zhang, L. Prebiotic synthesis of mineral-bearing microdroplet from inorganic carbon photoreduction at air—water interface. *PNAS nexus* **2023**, *2* (11), No. pgad389.
- (12) Liang, Z.; Zhou, L.; Chan, C. K. Fast generation of peroxides via atmospheric particulate photosensitization. *Sci. Adv.* **2025**, *11* (40), No. eadr8776.
- (13) Wei, H.; Vejerano, E. P.; Leng, W.; Huang, Q.; Willner, M. R.; Marr, L. C.; Vikesland, P. J. Aerosol microdroplets exhibit a stable pH gradient. *Proc. Natl. Acad. Sci. U.S.A.* **2018**, 115 (28), 7272–7277.
- (14) Gong, K.; Ao, J.; Li, K.; Liu, L.; Liu, Y.; Xu, G.; Wang, T.; Cheng, H.; Wang, Z.; Zhang, X.; et al. Imaging of pH distribution inside individual microdroplet by stimulated Raman microscopy. *Proc. Natl. Acad. Sci. U.S.A.* **2023**, *120* (20), No. e2219588120.

- (15) Zhu, C.; Kumar, M.; Zhong, J.; Li, L.; Francisco, J. S.; Zeng, X. C. New Mechanistic Pathways for Criegee–Water Chemistry at the Air/Water Interface. *J. Am. Chem. Soc.* **2016**, *138* (35), 11164–11169.
- (16) Meng, Y.; Gnanamani, E.; Zare, R. One-Step Formation of Pharmaceuticals Having a Phenylacetic Acid Core Using Water Microdroplets. *J. Am. Chem. Soc.* **2023**, *145*, 7724–7728.
- (17) Zhu, C.; Kais, S.; Zeng, X. C.; Francisco, J. S.; Gladich, I. Interfaces Select Specific Stereochemical Conformations: The Isomerization of Glyoxal at the Liquid Water Interface. *J. Am. Chem. Soc.* **2017**, *139* (1), 27–30.
- (18) Bolei, C.; Xia, Y.; He, R.; Sang, H.; Zhang, W.; Li, J. L.; Chen, L.; Wang, P.; Guo, S.; Yin, Y.; Hu, L.; Song, M.; Liang, Y.; Wang, Y.; Jiang, G.; Zare, R. Water-solid contact electrification causes hydrogen peroxide production from hydroxyl radical recombination in sprayed microdroplets. *Proc. Natl. Acad. Sci. U.S.A.* **2022**, 119, No. e2209056119.
- (19) Zhu, C.; Zeng, X. C.; Francisco, J. S.; Gladich, I. Hydration, Solvation, and Isomerization of Methylglyoxal at the Air/Water Interface: New Mechanistic Pathways. J. Am. Chem. Soc. 2020, 142 (12), 5574–5582.
- (20) Meng, Y.; Gnanamani, E.; Zare, R. Direct C(sp3)-N Bond Formation between Toluene and Amine in Water Microdroplets. *J. Am. Chem. Soc.* **2022**, *144*, 19709–19713.
- (21) Wan, Z.; Fang, Y.; Liu, Z.; Francisco, J. S.; Zhu, C. Mechanistic Insights into the Reactive Uptake of Chlorine Nitrate at the Air—Water Interface. *J. Am. Chem. Soc.* **2023**, *145* (2), 944–952.
- (22) Song, X.; Meng, Y.; Zare, R. Spraying Water Microdroplets Containing 1,2,3-Triazole Converts Carbon Dioxide into Formic Acid. J. Am. Chem. Soc. 2022, 144, 16744–16748.
- (23) Zhong, J.; Zhu, C.; Li, L.; Richmond, G. L.; Francisco, J. S.; Zeng, X. C. Interaction of SO₂ with the Surface of a Water Nanodroplet. *J. Am. Chem. Soc.* **2017**, *139* (47), 17168–17174.
- (24) Zhao, L.; Song, X.; Gong, C.; Zhang, D.; Wang, R.; Zare, R.; Zhang, X. Sprayed water microdroplets containing dissolved pyridine spontaneously generate pyridyl anions. *Proc. Natl. Acad. Sci. U.S.A.* **2022**, *119*, No. e2200991119.
- (25) Lee, J. K.; Walker, K. L.; Han, H. S.; Kang, J.; Prinz, F. B.; Waymouth, R. M.; Nam, H. G.; Zare, R. N. Spontaneous generation of hydrogen peroxide from aqueous microdroplets. *Proc. Natl. Acad. Sci. U.S.A.* **2019**, *116* (39), 19294–19298.
- (26) Li, K.; Guo, Y.; Nizkorodov, S. A.; Rudich, Y.; Angelaki, M.; Wang, X.; An, T.; Perrier, S.; George, C. Spontaneous dark formation of OH radicals at the interface of aqueous atmospheric droplets. *Proc. Natl. Acad. Sci. U.S.A.* **2023**, *120* (15), No. e2220228120.
- (27) Wan, Z. Y.; Zhu, C. Q.; Francisco, J. S. Molecular Insights into the Spontaneous Generation of Cl₂O in the Reaction of Cl₂ONO and HOCl at the Air-Water Interface. *J. Am. Chem. Soc.* **2023**, *145* (31), 17478–17484.
- (28) Rao, Z. P.; Li, X. J.; Fang, Y. G.; Francisco, J. S.; Zhu, C. Q.; Chu, C. H. Spontaneous Oxidation of Thiols and Thioether at the Air-Water Interface of a Sea Spray Microdroplet. *J. Am. Chem. Soc.* 2023, 145 (19), 10839–10846.
- (29) Shaik, S.; Danovich, D.; Joy, J.; Wang, Z.; Stuyver, T. Electric-field mediated chemistry: uncovering and exploiting the potential of (oriented) electric fields to exert chemical catalysis and reaction control. *J. Am. Chem. Soc.* **2020**, *142* (29), 12551–12562.
- (30) Shi, L.; LaCour, R. A.; Qian, N.; Heindel, J. P.; Lang, X.; Zhao, R.; Head-Gordon, T.; Min, W. Water structure and electric fields at the interface of oil droplets. *Nature* **2025**, *640*, 87–93.
- (31) You, W.; Li, K.; Ge, Q.; Liu, Y.; Wang, W.; Xiong, H.; Ao, J.; Wang, J.; Yang, L.; Wang, R.; et al. Breaking the Forever Bonds: Interface-Enhanced Superoxide Chemistry for Efficient PFOA Degradation. *Environ. Sci. Technol.* **2025**, *59* (35), 19068–19080.
- (32) Lo Nostro, P.; Ninham, B. W. Hofmeister phenomena: an update on ion specificity in biology. *Chem. Rev.* **2012**, *112* (4), 2286–2322
- (33) Ge, Q.; Liu, Y.; You, W.; Li, Y.; Wang, W.; Yang, L.; Xie, L.; Li, K.; Wang, L.; Ma, M.; Wang, R.; Wang, J.; Huang, T.; Wang, T.; Ruan, X.; Ji, M.; Zhang, L. Substantially improved efficiency and

- selectivity of carbon dioxide reduction by superior hydrated electronin microdroplet. Sci. Adv. 2025, 11, No. eadx5714.
- (34) Wang, W.; Liu, M.; Wang, T.; Song, Y.; Zhou, L.; Cao, J.; Hu, J.; Tang, G.; Chen, Z.; Li, Z.; et al. Sulfate formation is dominated by manganese-catalyzed oxidation of SO₂ on aerosol surfaces during haze events. *Nat. Commun.* **2021**, *12* (1), No. 1993.
- (35) Liu, Y. Y.; Ge, Q. Y.; Wang, T.; Zhang, R. F.; Li, K. J.; Gong, K. D.; Xie, L. F.; Wang, W.; Wang, L. Q.; You, W. B.; Ruan, X. J.; Shi, Z. C.; Han, J.; Wang, R. B.; Fu, H. B.; Chen, J. M.; Chan, C. K.; Zhang, L. W. Strong electric field force at the air/water interface drives fast sulfate production in the atmosphere. *Chem* **2024**, *10* (1), 330–351.
- (36) Rossignol, S.; Tinel, L.; Bianco, A.; Passananti, M.; Brigante, M.; Donaldson, D. J.; George, C. Atmospheric photochemistry at a fatty acid—coated air-water interface. *Science* **2016**, 353 (6300), 699—702.
- (37) Li, K.; You, W.; Zhu, Y.; Wang, W.; Wang, L.; Liu, Y.; Ge, Q.; Wang, T.; Wang, R.; Ruan, X.; et al. Strong Electric Fields on Water Microdroplets Enable Near-Unity Selectivity in H2O2 Photosynthesis. *J. Am. Chem. Soc.* **2025**, *147* (40), 36136–36145.
- (38) Wang, L.; Wen, L.; Xu, C.; Chen, J.; Wang, X.; Yang, L.; Wang, W.; Yang, X.; Sui, X.; Yao, L.; Zhang, Q. HONO and its potential source particulate nitrite at an urban site in North China during the cold season. *Sci. Total Environ.* **2015**, 538, 93–101.
- (39) Jungwirth, P.; Tobias, D. J. Specific ion effects at the air/water interface. *Chem. Rev.* **2006**, *106* (4), 1259–1281.
- (40) Benedict, K. B.; McFall, A. S.; Anastasio, C. Quantum yield of nitrite from the photolysis of aqueous nitrate above 300 nm. *Environ. Sci. Technol.* **2017**, *51* (8), 4387–4395.
- (41) Carena, L.; Zoppi, B.; Sordello, F.; Fabbri, D.; Minella, M.; Minero, C. Phototransformation of vanillin in artificial snow by direct photolysis and mediated by nitrite. *Environ. Sci. Technol.* **2023**, *57* (23), 8785–8795.
- (42) Lambe, A. T.; Cappa, C. D.; Massoli, P.; Onasch, T. B.; Forestieri, S. D.; Martin, A. T.; Cummings, M. J.; Croasdale, D. R.; Brune, W. H.; Worsnop, D. R.; Davidovits, P. Relationship between oxidation level and optical properties of secondary organic aerosol. *Environ. Sci. Technol.* **2013**, 47 (12), 6349–6357.
- (43) Ni, H.; Huang, R.-J.; Pieber, S. M.; Corbin, J. C.; Stefenelli, G.; Pospisilova, V.; Klein, F.; Gysel-Beer, M.; Yang, L.; Baltensperger, U.; et al. Brown carbon in primary and aged coal combustion emission. *Environ. Sci. Technol.* **2021**, *55* (9), 5701–5710.
- (44) El Mais, A. E. R.; D'Anna, B.; Drinovec, L.; Lambe, A. T.; Peng, Z.; Petit, J.-E.; Favez, O.; Aït-Aïssa, S.; Albinet, A. Insights into secondary organic aerosol formation from the day-and nighttime oxidation of polycyclic aromatic hydrocarbons and furans in an oxidation flow reactor. *Atmos. Chem. Phys.* **2023**, 23 (23), 15077–15096.
- (45) Xie, M.; Chen, X.; Hays, M. D.; Lewandowski, M.; Offenberg, J.; Kleindienst, T. E.; Holder, A. L. Light absorption of secondary organic aerosol: composition and contribution of nitroaromatic compounds. *Environ. Sci. Technol.* **2017**, *51* (20), 11607–11616.
- (46) Cui, Y.; Chen, K.; Zhang, H.; Lin, Y.-H.; Bahreini, R. Chemical Composition and Optical Properties of Secondary Organic Aerosol from Photooxidation of Volatile Organic Compound Mixtures. *ACS ES T Air* **2024**, *1* (4), 247–258.
- (47) Bali, K.; Banerji, S.; Campbell, J. R.; Bhakta, A. V.; Chen, L.-W. A.; Holmes, C. D.; Mao, J. Measurements of brown carbon and its optical properties from boreal forest fires in Alaska summer. *Atmos. Environ.* **2024**, 324, No. 120436.
- (48) Chen, K.; Hamilton, C.; Ries, B.; Lum, M.; Mayorga, R.; Tian, L.; Bahreini, R.; Zhang, H.; Lin, Y.-H. Relative Humidity Modulates the Physicochemical Processing of Secondary Brown Carbon Formation from Nighttime Oxidation of Furan and Pyrrole. *ACS ES T Air* **2024**, *1* (5), 426–437.
- (49) Jiang, H.; Frie, A. L.; Lavi, A.; Chen, J. Y.; Zhang, H.; Bahreini, R.; Lin, Y.-H. Brown carbon formation from nighttime chemistry of unsaturated heterocyclic volatile organic compounds. *Environ. Sci. Technol. Lett.* **2019**, *6* (3), 184–190.

- (50) Lin, P.; Liu, J.; Shilling, J. E.; Kathmann, S. M.; Laskin, J.; Laskin, A. Molecular characterization of brown carbon (BrC) chromophores in secondary organic aerosol generated from photo-oxidation of toluene. *Phys. Chem. Chem. Phys.* **2015**, *17* (36), 23312–23325.
- (51) Yang, Z. M.; Tsona, N. T.; George, C.; Du, L. Nitrogen-Containing Compounds Enhance Light Absorption of Aromatic-Derived Brown Carbon. *Environ. Sci. Technol.* **2022**, *56* (7), 4005–4016
- (52) Wang, Y.; Jorga, S.; Abbatt, J. Nitration of Phenols by Reaction with Aqueous Nitrite: A Pathway for the Formation of Atmospheric Brown Carbon. ACS Earth Space Chem. 2023, 7 (3), 632–641.
- (53) Mayorga, R. J.; Zhao, Z.; Zhang, H. Formation of secondary organic aerosol from nitrate radical oxidation of phenolic VOCs: Implications for nitration mechanisms and brown carbon formation. *Atmos. Environ.* **2021**, 244, No. 117910.
- (54) Cui, Y.; Frie, A. L.; Dingle, J. H.; Zimmerman, S.; Frausto-Vicencio, I.; Hopkins, F.; Bahreini, R. Influence of ammonia and relative humidity on the formation and composition of secondary brown carbon from oxidation of 1-methylnaphthalene and long-ifolene. ACS Earth Space Chem. 2021, 5 (4), 858–869.
- (55) Marrero-Ortiz, W.; Hu, M.; Du, Z.; Ji, Y.; Wang, Y.; Guo, S.; Lin, Y.; Gomez-Hermandez, M.; Peng, J.; Li, Y.; et al. Formation and optical properties of brown carbon from small α -dicarbonyls and amines. *Environ. Sci. Technol.* **2019**, *53* (1), 117–126.
- (56) Wong, J. P. S.; Tsagkaraki, M.; Tsiodra, I.; Mihalopoulos, N.; Violaki, K.; Kanakidou, M.; Sciare, J.; Nenes, A.; Weber, R. J. Atmospheric evolution of molecular-weight-separated brown carbon from biomass burning. *Atmos. Chem. Phys.* **2019**, *19* (11), 7319–7334
- (57) Wang, W.; Liu, Y.; Wang, T.; Ge, Q.; Li, K.; Liu, J.; You, W.; Wang, L.; Xie, L.; Fu, H.; et al. Significantly Accelerated Photosensitized Formation of Atmospheric Sulfate at the Air–Water Interface of Microdroplets. *J. Am. Chem. Soc.* **2024**, *146* (10), 6580–6590.
- (58) Yang, L.; Liu, Y.; Ge, Q.; Wang, J.; Wang, R.; You, W.; Wang, W.; Wang, T.; Zhang, L. Atmospheric Hydroxyl Radical Route Revealed: Interface-Mediated Effects of Mineral-Bearing Microdroplet Aerosol. J. Am. Chem. Soc. 2025, 147 (4), 3371–3382.
- (59) Li, L.-F.; Liu, P.; Huang, Q.; Zhang, X.; Chao, X.; Pang, S.; Wang, W.; Cheng, Y.; Su, H.; Zhang, Y.-H.; Ge, M. Rethinking urban haze formation: Atmospheric sulfite conversion rate scales with aerosol surface area, not volume. *One Earth* **2024**, *7* (6), 1082–1095.
- (60) Zhang, X.; Huang, Q.; Liu, Y.-X.; Yin, J.; Pang, S.-F.; Liu, P.; Zhang, Y.-H.; Ge, M. Microdroplet Surface Drives and Accelerates Proton-Controlled, Size-Dependent Nitrate Photolysis. *J. Am. Chem. Soc.* 2025, 147 (23), 19595–19601.
- (61) Gligorovski, S.; Strekowski, R.; Barbati, S.; Vione, D. Environmental implications of hydroxyl radicals (*OH). *Chem. Rev.* **2015**, *115* (24), 13051–13092.
- (62) Al-Abadleh, H. A.; Motaghedi, F.; Mohammed, W.; Rana, M. S.; Malek, K. A.; Rastogi, D.; Asa-Awuku, A. A.; Guzman, M. I. Reactivity of aminophenols in forming nitrogen-containing brown carbon from iron-catalyzed reactions. *Commun. Chem.* **2022**, *5* (1), No. 112.
- (63) Pang, H.; Zhang, Q.; Lu, X.; Li, K.; Chen, H.; Chen, J.; Yang, X.; Ma, Y.; Ma, J.; Huang, C. Nitrite-mediated photooxidation of vanillin in the atmospheric aqueous phase. *Environ. Sci. Technol.* **2019**, 53 (24), 14253–14263.
- (64) Go, B. R.; Lyu, Y.; Ji, Y.; Li, Y. J.; Huang, D. D.; Li, X.; Nah, T.; Lam, C. H.; Chan, C. K. Aqueous secondary organic aerosol formation from the direct photosensitized oxidation of vanillin in the absence and presence of ammonium nitrate. *Atmos. Chem. Phys.* **2022**, 22 (1), 273–293.
- (65) Cai, M.; Zhao, Z.; Li, X.; Wang, G.; Yang, Y.; Zhao, W.; Wang, B.; Yang, H.; Chen, K.; Ge, S.; et al. Aqueous-Phase Photooxidation of Vanillin in the Presence of Nitrite: Characteristics, Products, and Mechanism. ACS ES T Air 2024, 1 (8), 860–870.

- (66) Zhang, Y.; Forrister, H.; Liu, J.; Dibb, J.; Anderson, B.; Schwarz, J. P.; Perring, A. E.; Jimenez, J. L.; Campuzano-Jost, P.; Wang, Y.; et al. Top-of-atmosphere radiative forcing affected by brown carbon in the upper troposphere. *Nat. Geosci.* **2017**, *10* (7), 486–489.
- (67) Gilardoni, S.; Massoli, P.; Paglione, M.; Giulianelli, L.; Carbone, C.; Rinaldi, M.; Decesari, S.; Sandrini, S.; Costabile, F.; Gobbi, G. P.; et al. Direct observation of aqueous secondary organic aerosol from biomass-burning emissions. *Proc. Natl. Acad. Sci. U.S.A.* **2016**, *113* (36), 10013–10018.
- (68) Wang, Q.; Song, Y.; Yuan, S.; Zhu, Y.; Wang, W.; Chu, L. Prodrug activation by 4, 4'-bipyridine-mediated aromatic nitro reduction. *Nat. Commun.* **2024**, *15* (1), No. 8643.
- (69) Fang, Z.; Lai, A.; Cai, D.; Li, C.; Carmieli, R.; Chen, J.; Wang, X.; Rudich, Y. Secondary Organic Aerosol Generated from Biomass Burning Emitted Phenolic Compounds: Oxidative Potential, Reactive Oxygen Species, and Cytotoxicity. *Environ. Sci. Technol.* **2024**, 58 (19), 8194–8206.
- (70) Li, Y.; Fu, T.-M.; Yu, J. Z.; Zhang, A.; Yu, X.; Ye, J.; Zhu, L.; Shen, H.; Wang, C.; Yang, X.; et al. Nitrogen dominates global atmospheric organic aerosol absorption. *Science* **2025**, 387 (6737), 989–995.
- (71) Li, K.; You, W.; Wang, W.; Gong, K.; Liu, Y.; Wang, L.; Ge, Q.; Ruan, X.; Ao, J.; Ji, M.; Zhang, L. Significantly accelerated photochemical perfluorooctanoic acid decomposition at the air—water interface of microdroplets. *Environ. Sci. Technol.* **2023**, *57* (50), 21448–21458.
- (72) Gonella, G.; Backus, E. H.; Nagata, Y.; Bonthuis, D. J.; Loche, P.; Schlaich, A.; Netz, R. R.; Kühnle, A.; McCrum, I. T.; Koper, M. T.; et al. Water at charged interfaces. *Nat. Rev. Chem.* **2021**, *5* (7), 466–485.
- (73) Meng, Y.; Xia, Y.; Xu, J.; Zare, R. N. Spraying of water microdroplets forms luminescence and causes chemical reactions in surrounding gas. *Sci. Adv.* **2025**, *11* (11), No. eadt8979.
- (74) Ge, Q.; Liu, Y.; Li, K.; Xie, L.; Ruan, X.; Wang, W.; Wang, L.; Wang, T.; You, W.; Zhang, L. Significant Acceleration of Photocatalytic CO₂ Reduction at the Gas-Liquid Interface of Microdroplets. *Angew. Chem., Int. Ed.* **2023**, 62 (27), No. e202304189.
- (75) Mack, J.; Bolton, J. R. Photochemistry of nitrite and nitrate in aqueous solution: a review. *J. Photochem. Photobiol. A* **1999**, *128* (1), 1–13.
- (76) Berkowitz, J.; Chupka, W.; Gutman, D. Electron affinities of O₂, O₃, NO, NO₂, NO₃ by endothermic charge transfer. *J. Chem. Phys.* **1971**, 55 (6), 2733–2745.
- (77) Souri, A. H.; Johnson, M. S.; Wolfe, G. M.; Crawford, J. H.; Fried, A.; Wisthaler, A.; Brune, W. H.; Blake, D. R.; Weinheimer, A. J.; Verhoelst, T.; et al. Characterization of errors in satellite-based HCHO/NO₂ tropospheric column ratios with respect to chemistry, column-to-PBL translation, spatial representation, and retrieval uncertainties. *Atmos. Chem. Phys.* **2023**, 23 (3), 1963–1986.
- (78) Fernandez, B. O.; Ford, P. C. Nitrite catalyzes ferriheme protein reductive nitrosylation. *J. Am. Chem. Soc.* **2003**, 125 (35), 10510–10511.
- (79) Yang, D.; Liu, Q.; Wang, S.; Bozorg, M.; Liu, J.; Nair, P.; Balaguer, P.; Song, D.; Krause, H.; Ouazia, B.; et al. Widespread formation of toxic nitrated bisphenols indoors by heterogeneous reactions with HONO. *Sci. Adv.* **2022**, *8* (48), No. eabq7023.
- (80) Barik, A.; Priyadarsini, K. I.; Mohan, H. Redox reactions of 2-hydroxy-3-methoxybenzaldehyde (-vanillin) in aqueous solution. *Radiat. Phys. Chem.* **2004**, *70* (6), 687–696.
- (81) Wang, J.; Li, Z. Electric field modulated configuration and orientation of aqueous molecule chains. *J. Chem. Phys.* **2024**, *161* (9), No. 094305.
- (82) Wang, Z.; Li, Y.; Wu, C.; Tsang, S. C. E. Electric-/magnetic-field-assisted photocatalysis: Mechanisms and design strategies. *Joule* **2022**, *6* (8), 1798–1825.
- (83) Zang, Y.; Zou, Q.; Fu, T.; Ng, F.; Fowler, B.; Yang, J.; Li, H.; Steigerwald, M. L.; Nuckolls, C.; Venkataraman, L. Directing isomerization reactions of cumulenes with electric fields. *Nat. Commun.* **2019**, *10* (1), No. 4482.

- (84) Gong, K.; Nandy, A.; Song, Z.; Li, Q.-S.; Hassanali, A.; Cassone, G.; Banerjee, S.; Xie, J. Revisiting the enhanced chemical reactivity in water microdroplets: The case of a diels—alder reaction. *J. Am. Chem. Soc.* **2024**, *146* (46), 31585—31596.
- (85) Jing, X.; Chen, Z.; Huang, Q.; Liu, P.; Zhang, Y.-H. Spatiotemporally resolved pH measurement in aerosol microdroplets undergoing chloride depletion: An application of in situ Raman microspectrometry. *Anal. Chem.* **2022**, *94* (43), 15132–15138.
- (86) Bain, A.; Lalemi, L.; Dawes, N. C.; Miles, R. E.; Prophet, A. M.; Wilson, K. R.; Bzdek, B. R. Surfactant partitioning dynamics in freshly generated aerosol droplets. *J. Am. Chem. Soc.* **2024**, *146* (23), 16028–16038.
- (87) Mao, Y.; Yu, B.; Wang, P.; Yue, S.; Zhan, S. Efficient reduction-oxidation coupling degradation of nitroaromatic compounds in continuous flow processes. *Nat. Commun.* **2024**, *15* (1), No. 6364.
- (88) Senande-Rivera, M.; Insua-Costa, D.; Miguez-Macho, G. Spatial and temporal expansion of global wildland fire activity in response to climate change. *Nat. Commun.* **2022**, *13* (1), No. 1208.

